

**Beyond modelocking: High repetition-rate frequency
combs derived from a continuous-wave laser**

by

Daniel C. Cole

B.S., Washington University in St. Louis, 2012

M.S., University of Colorado, 2015

A thesis submitted to the
Faculty of the Graduate School of the
University of Colorado in partial fulfillment
of the requirements for the degree of
Doctor of Philosophy
Department of Physics

2018

This thesis entitled:
Beyond modelocking: High repetition-rate frequency combs derived from a continuous-wave laser
written by Daniel C. Cole
has been approved for the Department of Physics

Scott A. Diddams

Reader Two

Date _____

The final copy of this thesis has been examined by the signatories, and we find that both the content and the form meet acceptable presentation standards of scholarly work in the above mentioned discipline.

Cole, Daniel C. (Ph.D., Physics)

Beyond modelocking: High repetition-rate frequency combs derived from a continuous-wave laser

Thesis directed by Dr. Scott A. Diddams

Optical frequency combs based on modelocked lasers have revolutionized precision metrology by facilitating measurements of optical frequencies, with implications both for fundamental scientific questions and for applications such as fast, broadband spectroscopy. In this thesis, I describe advances in the generation of frequency combs without modelocking in platforms with smaller footprints and higher repetition rates, with the ultimate goal of bringing frequency combs to new applications in a chip-integrated package. I discuss two approaches for comb generation: parametric frequency conversion in Kerr microresonators and active electro-optic modulation of a continuous-wave laser. After introducing microresonator-based frequency combs (microcombs), I discuss two specific developments in microcomb technology: First, I describe a new, extremely reliable method for generation of soliton pulses through the use of a phase-modulated pump laser. This technique eliminates the dependence on initial conditions that was formerly a universal feature of these experiments, presenting a solution to a significant technical barrier to the practical application of microcombs. Second, I present observations of *soliton crystal* states with highly structured ‘fingerprint’ optical spectra that correspond to ordered pulse trains exhibiting crystallographic defects. These pulse trains arise through interaction of solitons with avoided mode-crossings in the resonator spectrum. I also discuss generation of Kerr soliton combs in the Fabry-Perot (FP) geometry, with a focus on the differences between the FP geometry and the ring geometry that has been the choice of most experimenters to date. Next, I discuss combs based on electro-optic modulation. I introduce the operational principle, and then describe the first self-referencing of a frequency comb of this kind and a proof-of-principle application experiment. Finally, I discuss a technique for reducing the repetition rate of a high repetition-rate frequency comb, which will be a necessary post-processing step for some applications.

Contents

1	Introduction to microresonator-based frequency combs	1
1.1	Optical microring resonators	1
1.1.1	Resonant enhancement in a microring resonator	3
1.1.2	Thermal effects in microresonators	4
1.2	Microring resonator Kerr frequency combs	6
1.2.1	A model for Kerr-comb nonlinear optics: The Lugiato-Lefever equation	7
1.3	Description of Kerr-comb outputs using the Lugiato-Lefever equation	8
1.3.1	Analytical investigation of the resonator's CW response	8
1.3.2	Kerr comb outputs: extended modulation-instability patterns	11
1.3.3	Kerr comb outputs: solitons	13
A	Derivation of the Lugiato-Lefever equation from the nonlinear Schrodinger equation	18
	References	20

Figures

1.1	Optical microdisk resonator	2
1.2	Thermal bistability in microresonators	5
1.3	An illustration of four-wave mixing and frequency-comb generation.	6
1.4	Solution space for the Lugiato-Lefever equation	9
1.5	Investigation of the circulating CW power in a Kerr resonator	10
1.6	Extended-pattern solutions to the LLE	12
1.7	Soliton solutions to the LLE	14
1.8	Kerr-soliton energy-level diagram	16

Chapter 1

Introduction to microresonator-based frequency combs

This chapter introduces the basic physics of optical frequency-comb generation in Kerr-nonlinear microring resonators, with a particular emphasis on providing context for the results described in the subsequent chapters. This field emerged in 2007 with the first report of comb generation in silica microtoroids [1], and has evolved rapidly. There are facets to the field that are not discussed here; we note that a number of papers that review this topic have been published, each of which provides a unique perspective [2–5]. The combs generated in Kerr-nonlinear ring resonators, excluding those generated in definitively ‘macro’ fiber loops, have generally been called microcombs, despite the fact that some of the resonators used to generate them have dimensions on the scale of several millimeters. Microcombs are an attractive technology because of their high repetition rates and small footprints, especially relative to modelocked-laser-based combs, which make them promising candidates for inclusion in integrated photonics systems. Microcomb generation has been reported in a variety of platforms, including the aforementioned silica microtoroids, silica wedge [6, 7] and rod [8] resonators, crystalline magnesium-fluoride [9] and calcium-fluoride [10] resonators, and silicon-nitride waveguide resonators [11, 12], which have the advantage of being immediately amenable to photonic integration.

For simplicity, and following the terminology of the field, we will refer to broadband optical spectra generated through frequency conversion in Kerr-nonlinear microring resonators as ‘Kerr combs,’ even when the output is not strictly a coherent frequency comb. Finally, we note that although researchers have so far focused on Kerr-comb generation with the ring geometry, it is also possible to generate Kerr combs in a Kerr-nonlinear Fabry-Perot (FP) cavity, as has been demonstrated in several experiments [13, 14]. Theoretical investigations of Kerr-comb generation with the FP geometry are presented in Chapter ??.

1.1 Optical microring resonators

An optical microring resonator guides light for many round trips around a closed path in a dielectric medium by total internal reflection. The principle is the same as the guiding of light in an optical fiber, and indeed a ‘macroring’ resonator can be constructed from a loop of fiber, using a fiber-optic coupler with a small coupling ratio as an input/output port. Microring resonators can be constructed by looping an optical waveguide back on itself, in which case the resonator provides index contrast and light confinement over a full 360° of the modal cross-section. Alternatively, resonators can be realized with geometries that lack an inner radius dimension and therefore provide less spatial confinement. In this case they can host ‘whispering-gallery modes,’¹ so-called due to their similarity with the acoustic ‘whispering-gallery’ waves that permit a listener on one side of St. Paul’s cathedral (for example) to hear whispers uttered by a speaker on the other side of the cathedral. A schematic

¹ In some sources the terminology ‘whispering-gallery mode resonator’ has been applied more generally, but the analogy to the acoustic case seems most appropriate for resonators in which index contrast is not provided over a full 360° of the modal cross-section. Otherwise it is unclear what makes a WGM resonator different from a fiber loop, which in the limit of large radius obviously does not host whispering-gallery modes. This issue of terminology is discussed in Ref. [15].

depiction of the basic components of a typical microring-resonator experiment is shown in Fig. 1.1. Optical microring resonators have a host of characteristics that make them useful for photonics applications in general and for nonlinear optics in particular; these include the ease with which they can be integrated and the ability to tailor the spectral distribution of guided modes through careful resonator design, as well as the ultra-high quality factors that have been demonstrated (\geq several hundred million). The resonator quality factor Q is defined as $Q = \omega_0 \tau_{ph} = \nu_0 / \Delta\nu$, where $\omega_0 = 2\pi\nu_0$ is the optical angular frequency, τ_{ph} is the photon lifetime, and $\Delta\nu$ is the resonance linewidth. The Q can be interpreted literally as the optical phase that is traversed by the carrier wave during the photon lifetime and is a useful figure of merit for nonlinear optics.

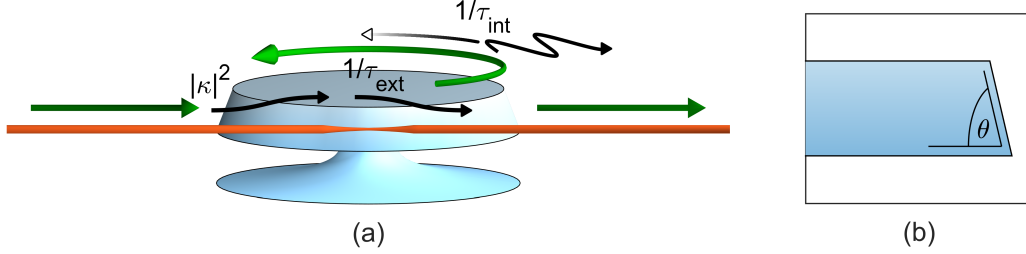


Figure 1.1: **Optical microdisk resonator.** (a) An optical microring resonator with the disk geometry as described in Ref. [6], operated in a through-coupled configuration. Light (green) is evanescently coupled into and out of the resonator through a tapered optical fiber, shown in orange, which contacts the resonator near the fiber's point of smallest diameter. Light circulates in whispering-gallery modes concentric to the resonator's circumference. The black labels indicate the coupling and loss rates discussed in Sec. 1.1.1: $|\kappa|^2$ is the rate at which incoming photons are coupled into the resonator, $1/\tau_{ext}$ is the rate at which circulating photons are coupling into the waveguide, and $1/\tau_{int}$ is the intrinsic loss rate. Here contributions to $1/\tau_{int}$ from absorption and radiative losses are depicted. (b) The wedge angle θ can be adjusted to control the geometric dispersion of the propagating whispering-gallery modes as described in Ref. [16], as θ dictates, for example, the extent to which larger (longer-wavelength) modes are confined further from the circumference of the wedge.

A microring resonator supports propagating guided modes of electromagnetic radiation with (vacuum) wavelengths that evenly divide the optical round-trip path length: $\lambda_m = n_{eff}(\lambda_m)L/m$, with associated resonance frequencies $\nu_m = c/\lambda_m = mc/n_{eff}(\nu_m)L$. This leads to constructive interference from round trip to round trip. Here m is the azimuthal mode number and the quantity $Ln_{eff}(\lambda_m)$ is the optical round-trip path length of the mode, where $n_{eff}(\lambda_m)$ defines an effective index of refraction related to the mode's propagation constant $k(\omega)$ via $k(\omega) = n_{eff}(\omega)\omega/c$ (see e.g. Refs. [17, 18]; we use the symbol k here and reserve the standard symbol β for another quantity). The free-spectral range f_{FSR} of a resonator is the *local* frequency spacing between modes, calculated via:

$$f_{FSR} \approx \frac{\nu_{m+1} - \nu_{m-1}}{2} \quad (1.1)$$

$$= \frac{\partial \nu_m}{\partial m} \quad (1.2)$$

$$= \frac{c}{n_{eff}(\nu)L} - \frac{mc}{n_{eff}^2(\nu)L} \frac{\partial n_{eff}}{\partial \nu} \frac{\partial \nu}{\partial m}, \quad (1.3)$$

so that, rearranging, we obtain:

$$f_{FSR} = \frac{c/L}{\left(n_{eff} + \nu \frac{\partial n_{eff}}{\partial \nu}\right)} = \frac{c}{n_g L} = 1/T_{RT}, \quad (1.4)$$

where $n_g = n_{eff} + \nu \frac{\partial n_{eff}}{\partial \nu}$ is the group velocity of the mode and T_{RT} is the mode's round-trip time. The effective index n_{eff} is frequency dependent due to both intrinsic material dispersion and geometric dispersion, where the latter results for example from different sampling of material properties for different wavelength-dependent mode areas. A frequency-dependent n_{eff} leads to a non-uniform spacing in the cavity modes in frequency despite the linearity of ν_m in m ; equivalently this results in a frequency dependence of n_g and f_{FSR} .

Depending on the design, microring resonators can support many transverse mode profiles, or just one. The former is typical of whispering-gallery-mode resonators that lack an inner radius, such as the wedge resonator shown in Fig. 1.1 or free-standing silica microrod resonators [8]; the latter can be readily achieved using chip-integrated single-mode photonic waveguides. For a given resonator geometry, to calculate the frequency-dependent effective index $n_{eff}(\nu)$, thereby enabling calculation of the resonance frequencies and wavelengths, one must solve Maxwell's equations for the resonator geometry. Except in special cases of high symmetry (e.g. a dielectric sphere [19]), this is typically done numerically using finite-element modeling tools like COMSOL. The modes of an optical resonator, both within a mode family defined by a transverse mode profile (such that they differ only by azimuthal mode number m) and between mode families, must be orthogonal [20], with no linear coupling between them.

1.1.1 Resonant enhancement in a microring resonator

The lifetime τ_{ph} of circulating photons in a resonator is fundamental to its fitness for applications. Generally, two processes lead to the loss of circulating photons: intrinsic dissipation that occurs at a rate $1/\tau_{int}$ and out-coupling to an external waveguide that occurs at a rate $1/\tau_{ext}$, leading to a total loss rate of $\tau_{ph}^{-1} = \tau_{ext}^{-1} + \tau_{int}^{-1}$. To understand the quantitative role of these parameters, we consider a cavity mode of frequency ω_0 and described by instantaneous amplitude $a(t)$ (normalized such that $|a|^2 = N$, the number of circulating photons) driven by a pump field with frequency ω_p and rotating amplitude $s \propto \exp(i\omega_p t)$ (normalized such that $|s|^2 = S$, the rate at which photons in the coupling waveguide pass the coupling port) that is in-coupled with strength κ . The equation of motion for such a system is [20]:

$$\frac{da}{dt} = i\omega_0 a - \left(\frac{1}{2\tau_{int}} + \frac{1}{2\tau_{ext}} \right) a + \kappa s, \quad (1.5)$$

and the rates that determine the evolution of a are shown schematically in Fig. 1.1. We can immediately solve this equation by assuming that $a \propto \exp(i\omega_p t)$, and we obtain:

$$a = \frac{\kappa s}{\left(\frac{1}{2\tau_{int}} + \frac{1}{2\tau_{ext}} \right) + i(\omega_p - \omega_0)}. \quad (1.6)$$

The coupling strength κ into the waveguide and the out-coupling rate $1/\tau_{ext}$ are related by $|\kappa|^2 = 1/\tau_{ext}$; one can arrive at this conclusion by considering the special case $1/\tau_{int} = 0$ and exploiting the time-reversal symmetry of the system under this condition [20]. By squaring Eq. 1.6 and inserting this relationship between κ and τ_{ext} , we find:

$$N = \frac{\Delta\omega_{ext} S}{\Delta\omega^2/4 + (\omega_p - \omega_0)^2}, \quad (1.7)$$

where we have defined the rates $\Delta\omega_{ext} = 1/\tau_{ext}$, $\Delta\omega_{int} = 1/\tau_{int}$, and $\Delta\omega = \Delta\omega_{ext} + \Delta\omega_{int}$. Two important observations can be drawn from Eq. 1.7: First, the cavity response is Lorentzian with a full-width at half-maximum (FWHM) linewidth that is related to the photon lifetime via $\tau_{ph} = 1/\Delta\omega$, and second, on resonance the number of circulating photons is related to the input rate by the factor $\Delta\omega_{ext}/\Delta\omega^2 \ll 1$. This factor is not yet the resonant enhancement, which we now

calculate by considering the circulating power $P = N\hbar\omega_p/T_{RT}$ on resonance (when $\omega_p = \omega_0$):

$$P = \frac{4\Delta\omega_{ext}P_{in}/T_{RT}}{\Delta\omega^2} \quad (1.8)$$

$$= \frac{2}{\pi}P_{in}\eta\mathcal{F}, \quad (1.9)$$

where $\mathcal{F} = 2\pi\tau_{ph}/T_{RT} = f_{FSR}/\Delta\nu$ is the resonator finesse, $\eta = \Delta\omega_{ext}/\Delta\omega$ is the coupling ratio, typically of order $\sim \frac{1}{2}$, and $P_{in} = \hbar\omega_p S$ is the power in the waveguide. Thus, the circulating power is approximately a factor \mathcal{F} greater than the input power. The combination of this resonant enhancement and a small cavity mode volume enables very large circulating optical intensities in high finesse resonators, which is important for the application of microresonators in nonlinear optics.

1.1.2 Thermal effects in microresonators

In a typical microresonator frequency-comb experiment, a frequency-tunable pump laser is coupled evanescently into and out of the resonator using a tapered optical fiber [21, 22] (for e.g. free-standing silica disc resonators) or a bus waveguide (for chip-integrated resonators, e.g. in silicon nitride rings). When spatial overlap and phase-matching ($n_{eff,res} \sim n_{eff,coupler}$ [23]) between the evanescent mode of the coupler and a whispering-gallery mode of the resonator is achieved, with the frequency of the pump laser close to the resonant frequency of that mode, light will build up in the resonator and the transmission of the pump laser past the resonator will decrease.

In any experiment in which a significant amount of pump light is coupled into a resonator, one immediately observes that the cavity resonance lineshape in a scan of the pump-laser frequency is not Lorentzian as expected from Eq. 1.7; plots of measured resonance lineshapes are shown in Fig. 1.2a. This is because the resonator heats as it absorbs circulating optical power. Associated with this change in temperature are changes in the mode volume and the refractive index, described respectively by the coefficient of thermal expansion $\partial V/\partial T$ and the thermo-optic coefficient $\partial n/\partial T$. For typical microresonator materials the thermo-optic effect dominates, and $\partial n/\partial T > 0$ leads to a decrease in the resonance frequency with increased circulating power in thermal steady state. Thus, for an adiabatic scan across the cavity resonance with decreasing laser frequency, as the laser approaches the resonance in frequency space and power is coupled into the resonator, the resonance frequency will begin to shift with the laser frequency, and a sawtooth-shaped resonance emerges.

The thermal dynamics related to $\partial n/\partial T$ and $\partial V/\partial T$ dictate the signs and values of detuning $\omega_0 - \omega_p$ that are readily accessible in experiment. Specifically, a calculation of the thermal dynamics of the system composed of the pump laser and the resonator reveals that when the pump laser with frequency ω_p is near the ‘cold-cavity’ resonance frequency of a given cavity mode $\omega_{0,cold}$ the resonance has three possible thermally-shifted resonance frequencies $\omega_{0,shifted}$ at which thermal steady state is achieved [24]. Generally, these points are:

- (1) $\omega_p > \omega_{0,shifted}$, blue detuning² with significant coupled power and thermal shift
- (2) $\omega_p < \omega_{0,shifted}$, red detuning with significant coupled power and thermal shift
- (3) $\omega_p \ll \omega_0$, red detuning with insignificant coupled power and insignificant thermal shift

These points are depicted schematically in Fig. 1.2b. Steady-state point (1) is experimentally important, because in the presence of pump-laser frequency and power fluctuations it leads to so-called thermal ‘self-locking.’ Specifically for steady-state point (1), this can be seen as follows:

- If the pump-laser power increases, the cavity heats, the resonance frequency decreases, the detuning increases, and the change in coupled power is minimized.
- If the pump-laser power decreases, the cavity cools, the resonance frequency increases, the detuning decreases, and the change in coupled power is minimized.

² Here we use the convention that the ‘color’ of the detuning specifies the position of the laser with respect to the resonance—‘blue’ detuning means that the laser is more blue, or higher in frequency.

- If the pump-laser frequency increases, the cavity cools, the resonance frequency increases, and the change in coupled power is minimized.
- If the pump-laser frequency decreases, the cavity heats, the resonance frequency decreases, and the change in coupled power is minimized.

This is in contrast with steady-state point (2), where each of the four pump-laser fluctuations considered above generates a positive feedback loop, with the result that any fluctuation will push the system towards point (1) or point (3) and so point (2) is unstable. This preference of the system to occupy point (1) or point (3) over a range of pump-laser detuning is referred to as thermal bistability. As a result of this bistability, point (2) (i.e. red detuning with significant coupled power) cannot be observed in an experimental scan of the pump laser across the resonance in either direction. As explained above, when the pump-laser frequency is decreased the resonance takes on a broad sawtooth shape, while in an increasing-frequency scan the resonance takes on a narrow pseudo-Lorentzian profile whose exact shape depends on the scan parameters relative to the thermal timescale. A second consequence is that, in the absence of other stabilizing effects, operation at red detuning with significant coupled power in a microresonator experiment requires special efforts to mitigate the effects of thermal instability.

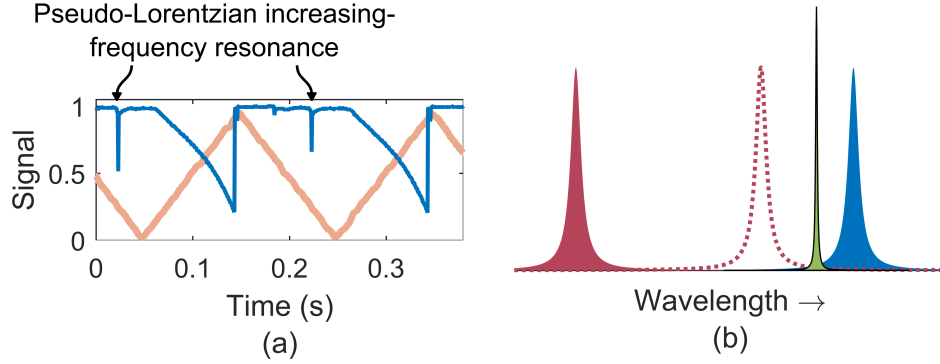


Figure 1.2: Thermal bistability in microresonators. (a) Measurement of power transmitted past the microresonator (blue) in an experiment using a ~ 16.5 GHz-FSR microdisk resonator and a tapered fiber. The wavelength of the pump laser is controlled by a piezo-electric crystal that adjusts the length of the laser cavity. Here, larger control signal (orange) corresponds to longer laser wavelength. As the laser wavelength is increased, the resonator heats and a sawtooth-shaped resonance is observed. Ultimately the resonator reaches a maximum temperature that depends on the pump power, and the laser then becomes red-detuned as the wavelength continues to increase; then the resonator rapidly cools and the resonance is lost. Shortly thereafter, the direction of the scan is reversed. As the resonator wavelength is decreased, the system will ‘flip’ from steady-state point (3) to steady-state point (1), leading to observation of a narrow pseudo-Lorentzian resonance, with the exact shape depending on the thermal and scanning timescales. (b) Depiction of the three steady-state points for the laser detuning. For fixed laser wavelength (green), stable steady-state points exist with relatively small blue detuning and significant coupled power (solid blue), and relatively large red detuning and little coupled power (solid red). An unstable steady-state point also exists with red detuning and significant coupled power (dashed red). Note in this terminology that the color of the detuning (red or blue) refers to the position of the laser relative to the position of the resonance in wavelength space.

1.2 Microring resonator Kerr frequency combs

The high circulating optical intensities accessible in resonators with long photon lifetimes find immediate application in the use of microresonators for nonlinear optics. The experiments described in this thesis are conducted in silica microresonators. Silica falls into a broader class of materials that exhibit both centro-symmetry, which dictates that the second-order nonlinear susceptibility $\chi^{(2)}$ must vanish, and a significant third-order susceptibility $\chi^{(3)}$. The n^{th} -order susceptibility is a term in the Taylor expansion describing the response of the medium's polarization to an external electric field [25]: $P = P_0 + \epsilon_0\chi^{(1)}E + \epsilon_0\chi^{(2)}E^2 + \epsilon_0\chi^{(3)}E^3 + \dots$. The effect of $\chi^{(3)}$ can be described in a straightforward way as a dependence of the refractive index on the local intensity [17],

$$n = n_0 + n_2 I \quad (1.10)$$

where $n_2 = \frac{3\chi^{(3)}}{4n_0^2\epsilon_0 c}$ is called the Kerr index [17, 26]. The intensity-dependence of the refractive index resulting from the third-order susceptibility $\chi^{(3)}$ is referred to as the optical Kerr effect and enables the self-phase modulation, cross-phase modulation, and four-wave mixing (FWM) nonlinear processes, the last of which is depicted schematically in Fig. 1.3 [25].

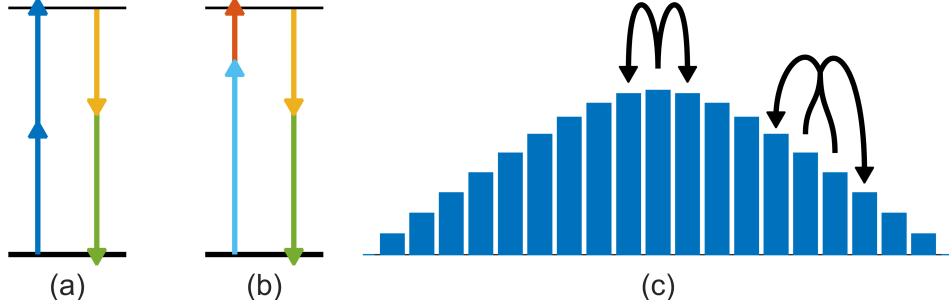


Figure 1.3: **An illustration of four-wave mixing and frequency-comb generation.** (a) Degenerate four-wave mixing, in which two fields of the same frequency ω_1 (blue) mix and generate fields at two new frequencies ω' and ω'' (yellow and green). The schematic indicates the energy-conservation requirements of the process, which can be written as $2\omega_1 = \omega' + \omega''$. (b) Non-degenerate four-wave mixing, in which two fields of different frequencies ω_2 and ω_3 (light blue and orange) mix to generate fields at frequencies ω' and ω'' (yellow and green). Energy conservation is now expressed as $\omega_2 + \omega_3 = \omega' + \omega''$. (c) Schematic depiction of one degenerate FWM step and one non-degenerate FWM step in a cascaded four-wave mixing process that generates a frequency comb. Figure after Ref. [2].

In 2007, a remarkable result brought about a new era for frequency comb research. Del'Haye et al. reported *cascaded four-wave mixing* (CFWM, shown in Fig. 1.3c) in anomalously-dispersive ($k'' = \frac{\partial^2}{\partial \omega^2} \frac{n_{eff}(\omega)\omega}{c} < 0$) toroidal silica microcavities on silicon chips, the result of which was a set of many co-circulating optical fields that were uniformly spaced by f_{rep} ranging from 375 GHz to ~ 750 GHz (depending on the platform) [1]. This result built on previous demonstrations of few-mode parametric oscillation in microresonators [27–29], and showed that the non-uniform distribution of cavity resonance frequencies due to dispersion could be overcome to generate an output with equidistant frequency modes. A second important development occurred in 2012, when Herr et al. reported the generation of frequency combs corresponding in the time domain to single circulating optical ‘soliton’ pulses [30, 31]. This observation followed the observation of solitons in formally-equivalent passive fiber-ring resonators in 2010 [32]. Due to unique properties that make them particularly well-suited for applications, as discussed in Sec. 1.3.3, the generation and manipulation of soliton combs has become a significant priority in microcomb research.

1.2.1 A model for Kerr-comb nonlinear optics: The Lugiato-Lefever equation

Kerr-comb generation can be motivated and partially understood through the CFWM picture [33], but the phase and amplitude degrees of freedom for each comb line mean that CFWM gives rise to a rich space of comb phenomena—it is now known that Kerr combs can exhibit several fundamentally distinct outputs. A useful model for understanding this rich space is the Lugiato-Lefever equation (LLE), which was shown to describe microcomb dynamics by Chembo and Menyuk [34] through Fourier-transformation of a set of coupled-mode equations describing CFWM and by Coen, Randle, Sylvestre, and Erkintalo [35] through time-averaging of a more formally-accurate model for a low-loss resonator (as first performed by Haelterman, Trillo, and Wabnitz [36]). The LLE is a nonlinear partial-differential equation that describes evolution of the normalized cavity field envelope ψ over a slow time $\tau = t/2\tau_{ph}$ in a frame parametrized by the ring's azimuthal angle θ (running from $-\pi$ to π) co-moving at the group velocity.³ I provide a derivation of the LLE in Appendix A. The equation in the notation of Chembo and Menyuk, as it will be used throughout this thesis, reads:

$$\frac{\partial \psi}{\partial \tau} = -(1 + i\alpha)\psi + i|\psi|^2\psi - i\frac{\beta_2}{2}\frac{\partial^2 \psi}{\partial \theta^2} + F. \quad (1.11)$$

This equation describes ψ over the domain $-\pi \leq \theta \leq +\pi$ with periodic boundary conditions $\psi(-\pi, \tau) = \psi(\pi, \tau)$. Here F is the field strength of the pump laser, with F and ψ both normalized so that they take the value 1 at the absolute threshold for parametric oscillation: $F = \sqrt{\frac{8g_0\Delta\omega_{ext}}{\Delta\omega^3}\frac{P_{in}}{\hbar\omega_p}}$, $|\psi|^2 = \frac{2g_0T_{RT}}{\hbar\omega_p\Delta\omega}P_{circ}(\theta, \tau)$, so that $|\psi(\theta, \tau)|^2$ is the instantaneous normalized power at the co-moving azimuthal angle θ . Here $g_0 = n_2c\hbar\omega_p^2/n_g^2V_0$ is a parameter describing the four-wave mixing gain, $\Delta\omega_{ext}$ is the rate of coupling at the input/output port, $\Delta\omega = 1/\tau_{ph}$ is the FWHM resonance linewidth, P_{in} is the pump-laser power, $P_{circ}(\theta, \tau)$ is the local circulating power in the cavity, \hbar is Planck's constant, and ω_p is the pump-laser frequency. The parameters n_2 , n_g , and V_0 describe the nonlinear (Kerr) index (see Eqn. 1.10), the group index of the mode, and the effective nonlinear mode volume at the pump frequency; L is the physical round-trip length of the ring cavity.

The parameters α and β_2 describe the frequency detuning of the pump laser and second-order dispersion of the resonator mode family into which the pump laser is coupled, both normalized to half the cavity linewidth:

$$\alpha = -\frac{2(\omega_p - \omega_0)}{\Delta\omega}, \quad (1.12)$$

$$\beta_2 = -\frac{2D_2}{\Delta\omega}; \quad (1.13)$$

here $D_2 = \left.\frac{\partial^2 \omega_\mu}{\partial \mu^2}\right|_{\mu=0}$ is the second-order modal dispersion parameter, where μ is the pump-referenced mode number of Eq. ???. The parameters $D_1 = \left.\frac{\partial \omega_\mu}{\partial \mu}\right|_{\mu=0} = 2\pi f_{FSR}$ and D_2 are related to the derivatives of the propagation constant $k(\omega) = \frac{n_{eff}(\omega)\omega}{c}$ via $D_1 = 2\pi/Lk'$ and $D_2 = -D_1^2 \frac{k''}{k'}$. It is useful to note that $k' = 1/v_g$, where v_g is the group velocity in the medium, and k'' is often referred to as the GVD parameter and denoted by β_2 , which here is reserved for the dispersion parameter in the LLE. Expressions for higher-order modal dispersion parameters D_n in terms of the expansion of the propagation constant can be obtained by evaluating the equation $D_{n>1} = (D_1 \frac{\partial}{\partial \omega})^{n-1} D_1$, and may be incorporated into the LLE up to desired order N through the replacement:

$$-i\frac{\beta_2}{2}\frac{\partial^2 \psi}{\partial \theta^2} \rightarrow + \sum_{n=1}^N i^{n+1} \frac{\beta_n}{n!} \frac{\partial^n \psi}{\partial \theta^n}, \quad (1.14)$$

³ The co-moving azimuthal angle θ is analogous to the ‘fast time’ variable that appears in, for example, the nonlinear Schrodinger equation for fiber-optic pulse propagation [17], and it can be transformed explicitly to a fast time t via $t = T_{RT} \times \frac{\theta}{2\pi}$.

where $\beta_n = -2D_n/\Delta\omega$. This thesis describes frequency-comb generation in anomalously-dispersive resonators, and so $\beta_2 < 0$ throughout.

The formulation of the LLE in terms of dimensionless normalized parameters helps to elucidate the fundamental properties of the system and facilitates comparison of results obtained in platforms with widely different experimental conditions. The LLE relates the time-evolution of the intracavity field (normalized to its threshold value for cascaded four-wave mixing) to the power of the pump laser (normalized to its value at the threshold for cascaded four-wave mixing), the pump-laser detuning (normalized to half the cavity linewidth), and the cavity second-order dispersion quantified by the change in the FSR per mode (normalized to half the cavity linewidth). One example of the utility of this formulation is that it makes apparent the significance of the cavity linewidth in determining the output comb, and underscores the fact that optimization of the dispersion, for example, without paying heed to the effect of this optimization on the cavity linewidth, may not yield the desired results. This adds an additional layer of complexity to dispersion engineering relative to straight waveguides.

The LLE is, of course, a simplified description of the dynamics occurring in the microresonator. It abstracts the nonlinear dynamics and generally successfully describes the various outputs that can be generated in a microresonator frequency comb experiment. The LLE is a good description of these nonlinear dynamics when the resonator photon lifetime, mode overlap, and nonlinear index n_2 are roughly constant over the bandwidth of the generated comb, and when the dominant contribution to nonlinear dynamics is simply the self-phase modulation term $i|\psi|^2\psi$ arising from the Kerr nonlinearity. The LLE neglects the polarization of the electric field (ψ is a scalar), as well as thermal effects and the Raman scattering and self-steepening nonlinearities, although in principle each of these can be included [17, 31, 37, 38]. It is also worth emphasizing that the LLE can be derived from a more formally-accurate Ikeda map (as explained by Coen et al. [35]), in which the effect of localized input- and output-coupling is included in the model. This derivation is accomplished by ‘delocalizing’ the pump field and the output-coupling over the round trip, including only their averaged effects. This is an approximation that is valid in the limit of high finesse due to the fact that the cavity field cannot change on the timescale of a single round trip, but as a result the LLE necessarily neglects all dynamics that might have some periodicity at the round-trip time; the fundamental timescale of LLE dynamics is the photon lifetime.

1.3 Description of Kerr-comb outputs using the Lugiato-Lefever equation

The LLE provides a useful framework for the prediction and interpretation of experimental results. Basically, it predicts the existence of two fundamentally distinct types of Kerr-combs: extended temporal patterns and localized soliton pulses. These predictions are born out by experiments, the interpretation of which is facilitated by insight gained from the LLE. In the remainder of this chapter I briefly present some analytical results that can be obtained from the LLE about the behavior of the continuous-wave (CW) field that exists in the resonator in the absence of Kerr-comb formation, and then discuss these two types of comb outputs. This discussion provides context for the results presented in the next two chapters. Fig. 1.4 summarizes the results that will be presented in the remainder of this chapter, and in particular shows the values of the parameters α and F^2 at which solitons and extended patterns can be obtained.

1.3.1 Analytical investigation of the resonator’s CW response

Some insight into comb dynamics can be obtained via analytical investigations of the LLE, Eq. 1.11. This section largely follows the analysis of Ref. [39], with similar analysis having been performed elsewhere, for example in Refs. [35] and [40]. When the derivative term $\partial^2\psi/\partial\theta^2$ in the LLE is non-zero, ψ is necessarily broadband, and a Kerr comb has been formed. There are no known exact analytical solutions to the LLE to describe Kerr-comb outputs, which must instead be numerically simulated (see Appendix ??). However, flat solutions ψ_{CW} to the LLE may be calculated

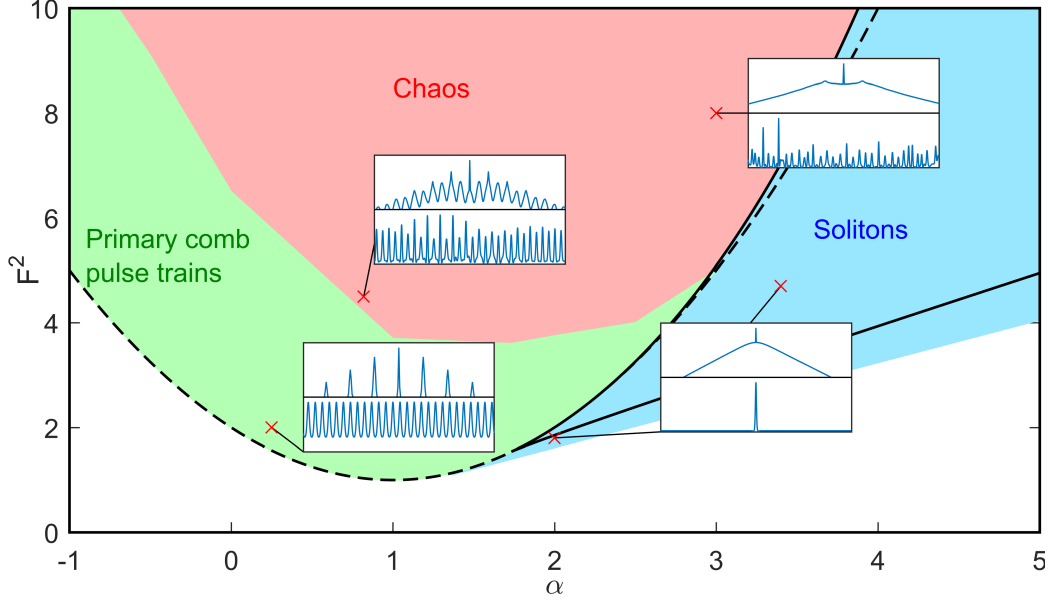


Figure 1.4: **Solution space for the Lugiato-Lefever equation.** Depiction of the various behaviors exhibited by ψ as a function of its position in the $\alpha - F^2$ plane; this predicts the type of Kerr-comb output as a function of the pump-laser detuning and power, the parameters that are most readily adjusted in experiment. Curves plotted in black are obtained through analytical investigation of the LLE; these include the threshold curve for parametric oscillation (dashed black, Eq. 1.21) and the lines obtained via $\rho(\alpha, F^2) = \rho_{\pm}(\alpha)$ (solid black, Eq. 1.18), which define the region where the LLE exhibits multiple flat solutions (i.e. solutions such that $\partial\psi/\partial\theta = 0$, Eq. 1.15). Extended patterns arise above the threshold curve through modulation instability. Solitons exist outside of the threshold curve at higher red detuning, up to an approximate maximum $\alpha_{max} = \pi^2 F^2/8$. The lines bounding the existence of chaos are not known precisely, and in fact chaos can be observed in simulation outside of the threshold curve at values $\alpha > \alpha_{thresh,+}$ (Eq. 1.22). Insets show representative simulation results for the various types of comb outputs in the frequency (top) and time (bottom) domains. Fig. after Ref. [39].

by setting all derivatives to zero—when these solutions can be realized physically (discussed below), they describe a CW field in the resonator. Upon setting the derivatives in the LLE to zero, one finds:

$$F = (1 + i\alpha)\psi_{CW} - i|\psi_{CW}|^2\psi_{CW}. \quad (1.15)$$

The circulating intensity $\rho = |\psi_{CW}|^2$ is obtained by taking the modulus-square of Eq. 1.15 to obtain:

$$F^2 = (1 + (\alpha - \rho)^2) \rho, \quad (1.16)$$

$$= \rho^3 - 2\alpha\rho^2 + (\alpha^2 + 1)\rho, \quad (1.17)$$

whereupon this equation can be numerically solved for ρ . As a third-order polynomial in ρ this equation has three solutions, one or three of which may be real; the complex solutions are unphysical. The function $F^2(\alpha, \rho)$ defined by this equation uniquely determines F^2 given α and ρ . We now consider plotting a graph of $F^2(\alpha, \rho)$ with α held constant; examples are given in Fig. 1.5. By noting that $F^2(\alpha, \rho = 0) = 0$ and $\partial F^2/\partial\rho|_{\rho=0} > 0$, we can conclude that a graph of $F^2(\alpha, \rho)$ will cross the same value F^2 three times if F^2 is between the extremal values $F_{\pm}^2(\alpha)$ at which $\partial F^2/\partial\rho = 0$. This means that three real solutions ρ_1 , ρ_2 , and ρ_3 for the inverted function $\rho(\alpha, F^2)$ exist for each value of F^2 between $F_-^2(\alpha)$ and $F_+^2(\alpha)$. The values $F_{\pm}^2(\alpha)$ bounding this region of degeneracy in ρ are found by inserting the values ρ_{\pm} at which $\partial F^2/\partial\rho = 0$ into Eq. 1.16. That is, $F_{\pm}^2(\alpha) = F^2(\alpha, \rho_{\mp})$,

where:

$$\rho_{\pm} = \frac{2\alpha \pm \sqrt{\alpha^2 - 3}}{3}. \quad (1.18)$$

For pump powers outside of the interval $[F_-^2(\alpha), F_+^2(\alpha)]$, which varies with α , there is only one real solution ρ ; within this interval there are three. This is illustrated in Fig. 1.5. The smallest value of F^2 at which the stationary curve ρ becomes multivalued is found to be $F^2 = 8\sqrt{3}/9$ by solving for $\rho_- = \rho_+$ and inserting the corresponding values into Eq. 1.16.

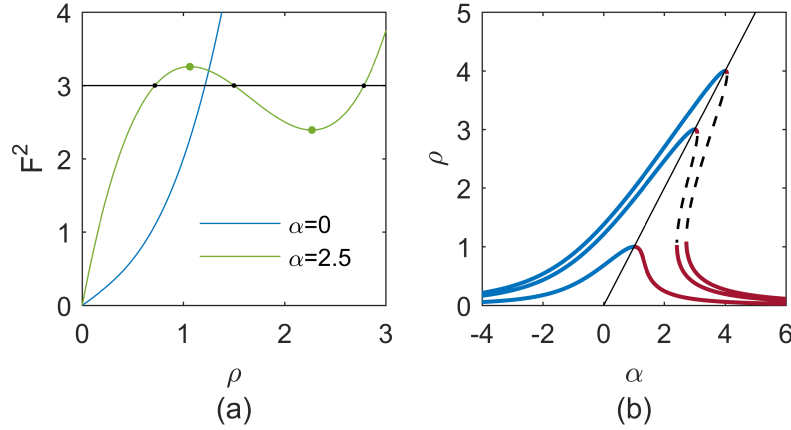


Figure 1.5: Investigation of the circulating CW power in a Kerr resonator. (a) Plots of F^2 as a function of ρ for $\alpha = 0$ (blue) and $\alpha = 2.5$ (green), according to Eq. 1.16. When real values of ρ exist that extremize F^2 according to this equation, multiple real solutions for the circulating power ρ exist between these extremal values of F^2 . For $\alpha = 2.5$ we indicate the extremal values of F^2 as green dots. For an example value $F^2 = 3$, the corresponding allowed values ρ_1 , ρ_2 , and ρ_3 are the intersections of the green curve and the black line (black dots); such a line would have three intersections with the green curve for any value of F^2 between $F_\alpha^2(\rho_-)$ and $F_\alpha^2(\rho_+)$. (b) Kerr-tilted resonances curves $\rho(\alpha)$ for $F^2 = 1$ (smallest), $F^2 = 3$, and $F^2 = 4$ (largest). The line $\rho = \alpha = F^2$ (solid black) marks the highest circulating power for a given input power F^2 and separates the effectively blue-detuned and effectively red-detuned branches. When $F^2 > 8\sqrt{3}/9$ (obtained by solving for $\rho_+ = \rho_-$, Eq. 1.18), the resonance becomes tilted steeply enough that an unstable middle branch (dashed black) exists.

Physically, the coexistence of multiple flat solutions ρ at a given point (α, F^2) corresponds to a ‘tilting’ of the Lorentzian transmission profile of the cavity and leads to bistability, even before taking into account thermal effects. This is illustrated in Fig. 1.5. For flat solutions ρ , an effective Kerr-shifted detuning can be defined as $\alpha_{eff} = \alpha - \rho$. The effective detuning simply incorporates the Kerr nonlinearity into the round-trip phase shift that describes the constructive or destructive interference of the circulating field with the pump at the coupling port. By noting that $\alpha = F^2 = \rho$ solves Eq. 1.16, we can conclude that the position of the effective Kerr-shifted resonance is on the line $\alpha = F^2$, where $\alpha_{eff} = 0$.

Once the circulating intensity ρ is known, the corresponding flat solution ψ_{CW} can be determined from Eq. 1.15 by inserting the known value of ρ and solving for ψ_{CW} , with the result:

$$\psi_{CW} = \frac{F}{1 + i(\alpha - \rho)}. \quad (1.19)$$

This expression reveals that the flat solution acquires a phase $\phi_s = \tan^{-1}(\rho - \alpha)$ relative to the pump.

If the flat solution(s) at a point (α, F^2) is (are) unstable, a Kerr comb will form spontaneously. Stability analysis of the flat solutions can be performed, and for the case of second-order dispersion alone the results are [39]:

- In the region of multi-stability, if the flat solutions are ordered with increasing magnitude as ρ_1 , ρ_2 , and ρ_3 , the middle solution ρ_2 is always unstable.
- When $\alpha < 2$, a flat solution ρ that is not the middle solution is stable if $\rho < 1$; otherwise it is unstable. When the flat solution is unstable, the mode that experiences the greatest instability has mode number given by:

$$\mu_{max} = \sqrt{\frac{2}{\beta_2}(\alpha - 2\rho)} \quad (1.20)$$

Therefore, the pump-laser threshold curve for Kerr-comb generation can be determined in the region $\alpha < 2$ of the $\alpha - F^2$ plane by setting $\rho = 1$ in Eq. 1.15:

$$F_{thresh}^2 = 1 + (\alpha - 1)^2, \quad (1.21)$$

$$\alpha_{thresh,\pm} = 1 \pm \sqrt{F^2 - 1}. \quad (1.22)$$

These equations explicitly describe the point at which comb is generated in an experiment in which the pump power or detuning is varied while the other is held fixed.

1.3.2 Kerr comb outputs: extended modulation-instability patterns

Extended temporal patterns arise spontaneously as a result of the instability of the flat solution to the LLE when the pump laser is tuned above the threshold curve. Two types of extended patterns are shown in Fig. 1.6. These patterns can be stationary, in which case they are typically referred to as ‘Turing patterns’ or ‘primary comb,’ or can evolve in time, in which case they are typically referred to as ‘noisy comb’ or ‘spatiotemporal chaos.’ In general, the former occurs for lower values of the detuning α and smaller pump strengths F^2 ; although some studies of the transition from Turing patterns to chaos have been conducted (e.g. Ref. [41]), a well-defined boundary between the two has not been established, and may not exist.

In the spatial domain parametrized by θ , a Turing pattern consists of a pulse train with (typically) $n \gg 1$ pulses in the domain $-\pi \leq \theta \leq \pi$ —the pulse train’s repetition rate is a multiple of the cavity FSR: $f_{rep} = n \times f_{FSR}$. Corresponding to the n -fold decreased period (relative to the round-trip time) of an n -pulse Turing pattern’s modulated waveform in the time domain, the optical spectrum of a Turing pattern consists of modes spaced by n resonator FSR—it is this widely-spaced spectrum that is referred to as ‘primary comb.’ Analytical approximations for Turing patterns are possible near threshold [42, 43] and in the small damping limit [44]. The stability analysis results from the last section can be used to predict the spacing n of a primary comb (equivalently the number of Turing-pattern pulses) generated in a decreasing-frequency scan across the resonance with fixed normalized pump power F^2 :

$$n = \mu_{max,thresh} = \sqrt{\Delta\omega_0(1 + \sqrt{F^2 - 1})/D_2}, \quad (1.23)$$

which is obtained by inserting $\alpha_{thresh,-}$ from Eq. 1.22 and $\rho = 1$ into the expression for μ_{max} in Eq. 1.20 above and moving to the dimensionful dispersion parameter D_2 . Fig. 1.6a shows measured and simulated primary comb spectra and Fig. 1.6b shows the corresponding simulated time-domain waveform.

Spatiotemporal chaos can be understood as a Turing pattern whose pulses oscillate in height, with adjacent pulses oscillating out of phase. From such an oscillating Turing pattern, if α and/or F^2 is increased, one moves deeper into the chaotic regime and pulses begin to exhibit lateral motion and collisions; the number of pulses present in the cavity is no longer constant in time. Depending

on the severity of the chaos (greater for larger α and F^2), a chaotic comb may correspond to a primary-comb-type spectrum with each primary-comb mode exhibiting sidebands at the resonator FSR, so-called ‘subcombs,’ or it may correspond to a spectrum with light in each cavity mode. Fig. 1.6c shows measured and simulated time-averaged spectra of chaotic combs and Fig. 1.6d shows a corresponding simulated time-domain waveform.

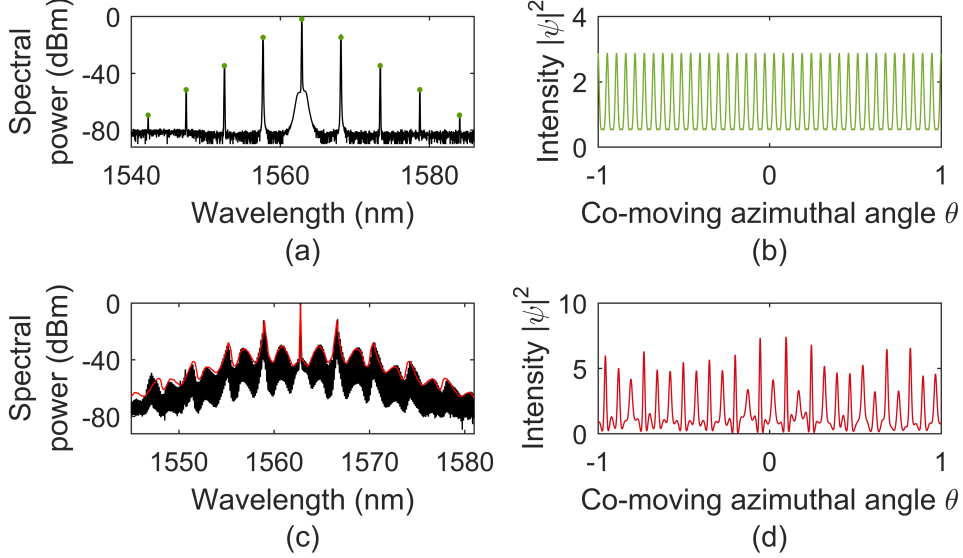


Figure 1.6: **Extended-pattern solutions to the LLE.** (a,b) Primary-comb pulse train in the frequency (a) and time (b) domains. The primary-comb spectrum corresponds to 39 time-domain pulses. The experimental optical spectrum (black) was obtained in a microdisk resonator with 17.32 GHz free-spectral range, and the simulation (green) is conducted with parameters near typical experimental values: $F^2=6$, $\alpha = -0.6$, and $\beta_2 = -0.0044$. (c,d) Spatiotemporal chaos obtained in the same resonator. The experimental measurement (black) yields a time-averaged optical spectrum, with a simulation of qualitatively similar dynamics shown in red. Simulation parameters are $F^2 = 4.2$, $\alpha = 1.2$, and $\beta_2 = -0.0054$. A snapshot of the evolving time-domain waveform is shown in (d).

Relative to generation of solitons, discussed below, experimental generation of an extended pattern is straightforward. These patterns are generated with blue effective pump-laser detuning $\alpha_{eff} < 0$, where thermal locking can occur. Because they arise spontaneously from noise, their generation is (comparatively) straightforward: simply decrease the pump-laser frequency until a pattern is generated. Unfortunately, operation of a Kerr-comb in the extended pattern regime is disadvantageous for applications: the n -FSR spacing of primary comb presents a challenge for measurement of the repetition rate of the frequency comb due to the bandwidth of measurement electronics and is also an inefficient use of physical space (i.e. for an n -pulse primary comb pulse train, an equivalent pulse train can always be obtained using the single-soliton output of a resonator with area that is smaller by a factor of $1/n^2$), and the aperiodic time-evolution of chaotic comb corresponds to modulation sidebands on the comb modes within the linewidth of the cavity that preclude the use of the comb as a set of stable optical reference frequencies.

An important property of these extended patterns is that they fill the resonator—the characteristic size of temporal features scales roughly as $1/\sqrt{-\beta_2}$, but these features are distributed densely and uniformly throughout the resonator. This means that the total circulating power of an extended pattern $\int d\theta |\psi|^2$ is large relative to the localized pulses discussed in the next section, and therefore that extended patterns come with a comparatively large thermal shift of the resonance.

As explained below, this contributes to the experimental challenges in soliton generation.

1.3.3 Kerr comb outputs: solitons

The term ‘soliton’ generally refers to a localized excitation that can propagate without changing its shape due to a delicate balance between dispersion (or diffraction) and nonlinearity; sometimes known as ‘solitary waves,’ solitons entered the scientific consciousness in the nineteenth century with their observation by John Scott Russell [45]. They are fundamental solutions to nonlinear partial-differential equations that describe a host of physical phenomena, and are found in several contexts within the field of nonlinear optics: spatial[42, 46] and spatiotemporal solitons (light bullets) [47] have been studied, and soliton modelocking [48, 49] is an important method of femtosecond pulse generation. Temporal Kerr-soliton pulses in optical fibers are particularly well known [17, 50], and have been considered as a candidate for fiber-optic communications protocols [51, 52]. Microresonators support so-called dissipative cavity solitons, which are localized pulses circulating the resonator that are out-coupled once per round trip. In the case of a single circulating soliton, this leads to a train of pulses propagating away from the resonator with repetition rate $1/T_{RT}$. Thus the mode spacing of the comb matches the FSR of the resonator, in contrast with widely-spaced primary comb spectra, and the soliton can, in principle, remain stable and propagate indefinitely as a stationary solution to the LLE. This makes Kerr combs based on solitons particularly attractive for applications.

1.3.3.1 Mathematical description of solitons

Solitons in optical fibers are solutions of the nonlinear Schrodinger equation (NLSE) that describes pulse-propagation in optical fiber [17]:

$$\frac{\partial A}{\partial z} = i\gamma|A|^2A - i\frac{\beta}{2}\frac{\partial^2 A}{\partial T^2}. \quad (1.24)$$

This equation describes the evolution of the pulse envelope A in the ‘fast-time’ reference frame parametrized by T as it propagates down the length of the fiber, parametrized by the distance variable z . Here $\gamma = \frac{2\pi}{\lambda} \frac{n_2}{A_{eff}}$ is the nonlinear coefficient of the fiber, where n_2 is the Kerr index, A_{eff} is the effective nonlinear mode area and λ is the carrier wavelength, and $\beta \equiv \beta_{prop,2}$ is the GVD parameter. The LLE can be viewed as an NLSE with additional loss and detuning terms $-(1+i\alpha)\psi$ and a driving term F .

The fundamental soliton solution to the NLSE is:

$$A_{sol} = \sqrt{P_0} \operatorname{sech}(T/\tau) e^{i\gamma P_0 z/2 + i\phi_0}, \quad (1.25)$$

where P_0 is the peak power of the pulse and is related to the duration of the pulse τ via $\tau = \sqrt{-\beta/\gamma P_0}$, and ϕ_0 is an arbitrary phase. Thus, this equation admits a *continuum* of pulsed fundamental ‘soliton’ solutions, with one existing for each value of the peak power. Each of these solutions propagates down the fiber without changing shape; only the phase evolves with distance as $\phi(z) = \gamma P_0 z/2 + \phi_0$.

The introduction of the loss, detuning, and driving terms into the NLSE to obtain the LLE has several important consequences for solitons. First, exact analytical expressions for the soliton solution to the LLE in terms of elementary functions are not known, in contrast with the situation for the NLSE. However, the soliton solutions to the LLE, Eq. 1.11, can be approximated well as:

$$\psi_{sol} = \psi_{CW,min} + e^{i\phi_0} \sqrt{2\alpha} \operatorname{sech} \sqrt{\frac{2\alpha}{-\beta_2}} \theta. \quad (1.26)$$

Here $\psi_{CW,min}$ is the flat solution to the LLE from Eq. 1.19 at the point where the soliton solution is desired; when multiple flat solutions exist, $\psi_{CW,min}$ is the one corresponding to the smallest intensity ρ_1 . The phase $\phi_0 = \cos^{-1}(\sqrt{8\alpha}/\pi F)$ arises from the intensity-dependent phase shift in the cavity

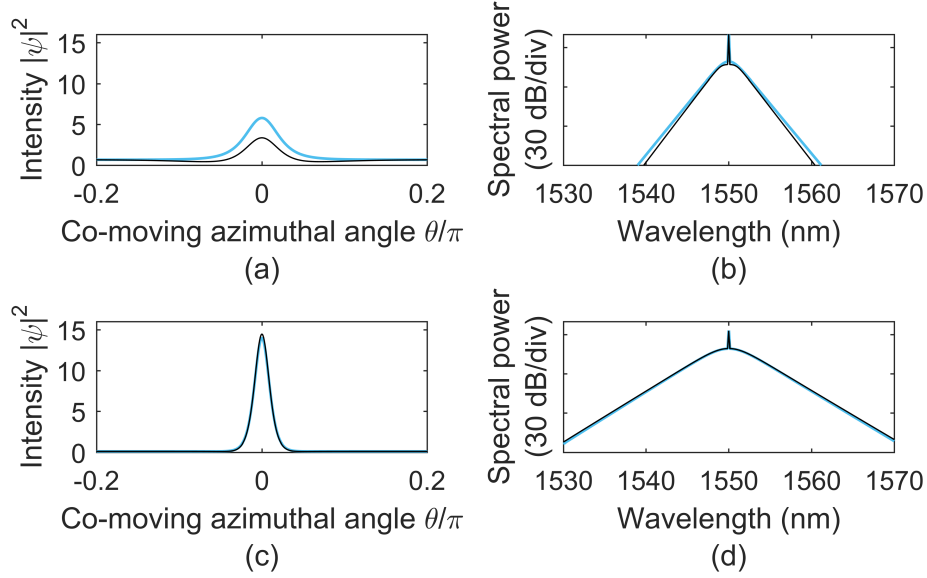


Figure 1.7: **Soliton solutions to the LLE.** Analytical approximations (color) and numerically-calculated exact solutions (black) to the LLE in the time (a,c) and frequency (b,d) domains. The solitons are calculated at $\alpha = 0.95 \alpha_{max} = 0.95 \pi^2 F^2 / 8$ for $F^2 = 8\sqrt{3}/9$ (a,b) and $F^2 = 6$ (c,d) with $\beta_2 = -0.02$ in both cases. The isolated spectral spike is at the pump frequency and corresponds to the CW background $\psi_{CW,min}$. Spectra are calculated using $f_{rep} = 16.5$ GHz with pump wavelength of $\lambda_p = 1550$ nm. For experimental measurements of solitons in microring resonators, see Chapters ?? and ??.

due to the Kerr effect, mathematically described by the term $i|\psi|^2\psi$. We depict this approximation, alongside numerical calculations of exact soliton solutions to the LLE, in Fig. 1.7.

This approximation ψ_{sol} from Eq. 1.26 for the soliton solution of the LLE illustrates a second important consequence of the differences between the NLSE and the LLE: while the NLSE admits a continuum of fundamental soliton solutions parametrized by their peak power P_0 and arbitrary phase ϕ_0 , the LLE supports only one shape for the envelope of a soliton for fixed experimental parameters. Intuitively, this can be understood as arising from the need for the round-trip phase shift for all points on the soliton to be zero in steady-state; the introduction of the detuning parameter α breaks the degeneracy that exists for the NLSE within the continuum of soliton solutions.

The analytical approximation in Eq. 1.26 indicates the scaling of the amplitude and width of the LLE soliton with the experimental parameters: the amplitude of the LLE soliton, prior to its summation with the CW background, depends only on the detuning α , and the width of the soliton increases with larger detuning α and smaller dispersion β_2 . Importantly, if one is concerned with maximizing the bandwidth of the soliton, it is important to minimize β_2 and maximize α , due to the inverse relationship between temporal duration and spectral bandwidth. The spectrum of a single-soliton Kerr comb has a $\text{sech}^2((\omega - \omega_p)/\Delta\omega_{sol})$ envelope, where ω is the optical angular frequency and $\Delta\omega_{sol} \approx \sqrt{32\alpha/|\beta_2|T_{RT}^2}$ is the bandwidth of the pulse in angular frequency. Equivalently, the bandwidth of the soliton in (linear) optical frequency is $\sqrt{\frac{16\Delta\nu f_{rep}^2}{D_2}\alpha}$, where $\Delta\nu$ is the resonance linewidth in linear frequency; the spectral width in mode number is $\Delta\mu_{sol} \approx 4\sqrt{\alpha\Delta\nu/D_2}$. Consistent with the phase ϕ_0 in the approximation ψ_{sol} in Eq. 1.26, solitons can exist up to a maximum detuning of $\alpha_{max} \sim \pi^2 F^2 / 8$ [31]. For a soliton at the maximum detuning for fixed normalized pump power F^2 , the bandwidth is then $\sqrt{\frac{\pi^2 \Delta\nu f_{rep}^2}{2D_2} F^2}$.

Solitons exist only where there is a stable flat solution ψ_{CW} that is effectively red detuned that can form the background for the pulse [40, 53]. This effectively red-detuned background is itself thermally unstable (see Sec. 1.1.2), but the existence of the soliton acts to stabilize the pump detuning. As explained by Herr et al., the soliton provides a local modulation of the refractive index through the Kerr effect, which changes the round-trip phase shift of pump light that arrives coincidentally with the soliton at the coupling port [31]. This leads to a *local* increase in the resonant wavelength for this pump light. Thus there are effectively two resonant wavelengths, a smaller one determined by the round-trip phase shift including the Kerr shift from the CW background, and a larger one determined by the round-trip phase shift including the Kerr shift from the soliton [54]. The pump laser can be effectively blue-detuned with respect to the latter resonance, which can lead to thermally stable operation in the soliton regime.

Solitons are strongly localized: as can be seen from Eq. 1.26, the deviation of the background intensity from ρ_1 near a soliton at θ_0 is proportional to $e^{-(\theta-\theta_0)/\delta\theta}$, where $\delta\theta = \sqrt{-\beta_2/2\alpha}$. If $\delta\theta$ is sufficiently small, multiple solitons can be supported in the resonator domain $-\pi \leq \theta \leq \pi$ with very weak interactions between solitons. If the separation between solitons i and j at θ_i and θ_j is small relative to $\delta\theta$, the solitons will interact. The topic of soliton interactions is complicated in general, with different types of interactions in different systems (see e.g. Refs. [55–58]). Simulations reveal that if $(\theta_i - \theta_j)/\delta\theta$ is too small, LLE solitons exhibit attractive interactions as a result of the monotonic (as opposed to oscillatory) decay of the localized pulse to ψ_{CW} [59], which precludes the existence of stable equilibrium separations. The result of this attraction can be pair-wise annihilation or merger, with the ultimate result being an ensemble with fewer solitons. The maximum number of solitons that can coexist in a resonator in the absence of higher-order stabilizing effects (see Chapter ?? and Refs. [59, 60]) can be approximated as $N_{max} \approx \sqrt{-2/\beta_2}$ [31]. An approximation to the form of a soliton ensemble is possible as:

$$\psi_{ens} = \psi_{CW,min} + e^{i\phi_0} \sqrt{2\alpha} \sum_j \text{sech} \left(\sqrt{\frac{2\alpha}{-\beta_2}} (\theta - \theta_j) \right), \quad (1.27)$$

where $\{\theta_j\}$ define the positions of the solitons in the ensemble and $\phi_0 = \cos^{-1}(\sqrt{8\alpha}/\pi F)$ as above. Fig. 1.8 provides an example illustrating the degeneracy in soliton number of Kerr-combs operating in the soliton regime.

1.3.3.2 Microresonator solitons in experiments

Relative to the generation of extended modulation-instability patterns, experimental generation of solitons in microring resonators is challenging. Solitons are localized excitations below threshold, which means that their existence is degenerate with their absence—a resonator can host $N = 0, 1, 2, \dots$ up to N_{max} solitons for a given set of parameters α and F^2 ; as discussed above and illustrated in Fig. 1.8. If α and F^2 are experimentally tuned to a point at which solitons may exist, ψ will evolve to a form determined by the initial conditions of the field ψ_0 . To provide initial conditions that evolve to $N > 0$ solitons, most experimental demonstrations of soliton generation have involved first generating an extended pattern in the resonator, and then tuning to an appropriate point (α, F^2) so that ‘condensation’ of solitons from the extended pattern occurs.

Condensation of solitons from an extended pattern presents additional challenges. First, it is difficult to control the number of solitons that emerge, due to the high degree of soliton-number degeneracy as shown in Fig. 1.8. This typically leads to a success rate somewhat lower than 100 % in the generation of single solitons. Second, the transition from a high duty-cycle extended pattern to a lower duty-cycle ensemble of one or several solitons comes with a dramatic drop in intracavity power that occurs on the timescale of the photon lifetime. If the resonator is in thermal steady-state before this drop occurs, the resonator will cool and the resonance frequency will increase. If this increase is large enough that the final detuning α exceeds $\alpha_{max} = \pi^2 F^2/8$, the soliton is lost. This challenge can be addressed by preparing initial conditions for soliton generation and then tuning to an appropriate point (α, F^2) faster than the cavity can come into thermal steady-state at the

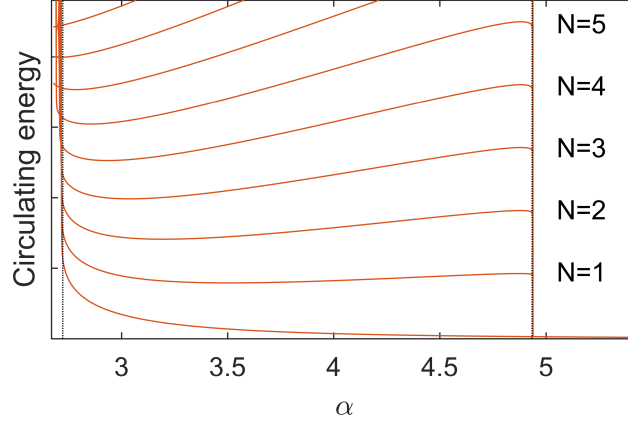


Figure 1.8: **Kerr-soliton energy-level diagram.** Some of the possible values of the circulating energy (proportional to $\int d\theta |\psi|^2$) in the soliton regime as a function of the detuning parameter α . Level curves correspond to the number of circulating solitons. This diagram is obtained from numerical solutions using $F^2 = 4$, $\beta_2 = -0.0187$, and is quantitatively dependent on both of these parameters. Dotted vertical lines indicate approximations to the minimum and maximum detunings for solitons. The approximation for the minimum detuning is the value of α at which the effectively red-detuned branch vanishes, obtained by inserting ρ_- (Eq. 1.18) into Eq. 1.16 for $F^2 = 4$ and solving for α , and the approximate maximum detuning is $\alpha_{max} = \pi^2 F^2 / 8$.

temperature determined by the larger power of the extended pattern; this is possible because the timescale over which an extended pattern can be generated is related to the photon lifetime, which is typically much faster than the thermal timescale.

The first report of soliton generation in microresonators came in 2012 in a paper by Herr et al. [31] (2012 pre-print [30]). These authors described optimizing the speed of a decreasing-frequency scan of the pump laser across the cavity resonance so that solitons could be condensed from an extended pattern and the scan could then be halted at a laser frequency where the solitons could be maintained with the system in thermal steady-state at the temperature determined by the circulating power of the solitons. Stochastic reduction in the number of solitons in the resonator after condensation from an extended pattern was identified in these experiments. This corresponds to transitions between levels in the diagram in Fig. 1.8, and is associated with discrete steps in a measurement of the ‘comb power,’ the output power of the resonator with the pump frequency ν_p filtered out. The resulting staircase-like nature of a comb power measurement is a useful experimental signature of soliton generation in microresonators, and is important for comparison with the results described in Chapter ??.

Other approaches for dealing with the challenges described above have been developed since this first demonstration; these include fast manipulation of the pump power [7, 61] or frequency [62], periodic modulation of the pump laser’s phase or power at f_{FSR} [14, 63], tuning of the cavity resonance frequency using chip-integrated heaters instead of tuning the pump-laser frequency [64, 65], and soliton-ensemble preparation and subsequent population reduction through manipulation of the pump laser [54]. These methods continue to make use of extended patterns to provide initial conditions for soliton generation. In formally-equivalent fiber-ring resonators, direct generation of solitons without condensation from an extended pattern has been demonstrated using transient phase and/or amplitude modulation of the pump laser [66–68].

1.3.3.3 Microresonator solitons in applications

Because solitons have single-FSR spacing, have the output localized into a high peak-power pulse, and are stationary (in contrast with chaos, which has single-FSR spacing but is not stationary), they are promising for applications. Many of the proposals for and demonstrations of applications with Kerr-combs have used single-soliton operation. Some of the applications already demonstrated include an optical clock [69], dual-comb spectroscopy [70], coherent communications [71], and direct on-chip optical frequency synthesis [72]. Additionally, soliton combs have been self-referenced both with [73, 74] and without [75, 76] external spectral broadening. Nevertheless, there remains work to be done to bring microresonator-soliton technology to the level of maturity that will be required for deployment in the field. Chapters ?? and ?? describe two recent advancements: the development of a method for direct on-demand generation of single solitons by use of a phase-modulated pump laser, and the observation and explanation of a soliton-interaction mechanism that imparts rigid structure on the allowed configurations of multi-soliton ensembles.

Appendix A

Derivation of the Lugiato-Lefever equation from the nonlinear Schrodinger equation

Here we show how the Lugiato-Lefever equation can be obtained by modeling propagation in a high-finesse ring cavity with the nonlinear Schrodinger equation. To my knowledge, the derivation given here was first performed by Haelterman, Trillo, and Wabnitz [36]. Our starting point is the NLSE for a pulse of restricted bandwidth such that higher-order nonlinearities are unimportant:

$$\frac{\partial A}{\partial z} = -\frac{\alpha_\ell}{2} A + i\gamma |A|^2 A - i \frac{k''}{2} \frac{\partial^2 A}{\partial T^2}. \quad (\text{A.1})$$

This equation is ubiquitous in the study of pulse propagation in Kerr-nonlinear media, and a derivation of it is provided, for example, in Ref. [17]. As discussed in Sec. 1.3.3.1, it describes the evolution of a pulse envelope A in a ‘fast-time’ reference frame parametrized by T as it propagates in a Kerr-nonlinear medium, where the propagation distance is parametrized by the variable z . Here $\gamma = \frac{2\pi}{\lambda} \frac{n_2}{A_{eff}}$ is the nonlinear coefficient of the medium, where n_2 is the Kerr index, A_{eff} is the effective nonlinear mode area and λ is the carrier wavelength, and $k'' = \frac{\partial}{\partial \omega} \frac{n_{eff}(\omega)\omega}{c}$ is the GVD parameter. Propagation loss described by the coefficient α_ℓ has been included in Eq. A.1.

The dynamics in a ring resonator constructed of a Kerr medium can be described by evolving the field envelope A over a round trip and then applying an operator that accounts for out-coupling of the circulating field A and in-coupling of a pump field A_{in} , as well as a round-trip phase shift ϕ_{RT} associated with the detuning of the carrier frequency from a cavity mode. This allows us to advance the field at the end of the n^{th} round trip $A_n(L, T)$ to the field $A_{n+1}(0, T)$ at the beginning of the $n + 1^{\text{th}}$ as:

$$A_{n+1}(0, T) = e^{i\phi_{RT}} \left(1 - \frac{T_{RT}}{2\tau_{ext}} \right) A_n(L, T) + \sqrt{\frac{T_{RT}}{\tau_{ext}}} A_{in}, \quad (\text{A.2})$$

where τ_{ext} describes in- and out-coupling as explained in Sec. 1.1.1 and $T_{RT} = L_{RT}/v_g$ is the round-trip time. If we define an operator $G_L(A)$ that advances the field over a distance L according to Eq. A.1 as $A(z + L, T) = G_L(A)A(z, T)$, then we have:

$$A_{n+1}(0, T) = e^{i\phi_{RT}} \left(1 - \frac{T_{RT}}{2\tau_{ext}} \right) G_L[A_n(0, T)] A_n(0, T) + \sqrt{\frac{T_{RT}}{\tau_{ext}}} A_{in}. \quad (\text{A.3})$$

The description of the field envelope in a Kerr-nonlinear ring cavity according to Eq. A.3 through iterated evolution according to the NLSE and then application of the in- and out-coupling operator is referred to as an Ikeda map [Ikeda1979]. We obtain the LLE by assuming that the operator $G_L(A) \approx 1$, that is, that the field does not evolve much over the round-trip length. This is equivalent to the assumption that the cavity length L_{RT} is much less than the length scales $L_\ell = 1/\alpha_\ell$, L_{NL} =and L_D =over which the terms on the right-hand side of Eq. A.1 lead to appreciable evolution of the pulse envelope.

We can write the operator G_L explicitly as:

$$G_L(A) = \left[1 + L \left(-\alpha_\ell/2 + i\gamma |A|^2 - i \frac{k''}{2} \frac{\partial^2}{\partial T^2} \right) \right]. \quad (\text{A.4})$$

here

here

We assume that each term in this operator besides the identity term is small. If we note that the round-trip phase shift ϕ_{RT} must also be small in a high-finesse cavity for appreciable build-up to occur, then we can expand the first term on the right-hand side of Eq. A.3 and retain only first order terms to find:

$$A_{n+1}(0, T) = \left(1 - \frac{T_{RT}}{2\tau_{ext}} + i\phi_{RT} - \frac{L\alpha_\ell}{2} + iL\gamma|A|^2 - iL\frac{k''}{2}\frac{\partial^2}{\partial T^2}\right) A_n(0, T) + \sqrt{\frac{T_{RT}}{\tau_{ext}}} A_{in}. \quad (\text{A.5})$$

By replacing n with the slow time $t = nT_{RT}$ and allowing t to vary continuously we arrive at a Lugiato-Lefever equation, albeit in a different form from the one presented in Eq. 1.11:

$$T_{RT}\frac{\partial A}{\partial t} = \left(-T_{RT}/2\tau_{ext} + i\phi_{RT} - L\alpha_\ell/2 + iL\gamma|A|^2 - iL\frac{k''}{2}\frac{\partial^2}{\partial T^2}\right) A + \sqrt{\frac{T_{RT}}{\tau_{ext}}} A_{in}. \quad (\text{A.6})$$

To recast this equation in the form used in the body of the thesis, we first pass to the normalized temporal and spatial variables τ and θ and the parameters α and β_2 . We note that $L\alpha_\ell/2 = T_{RT}/2\tau_{int}$ and define $\theta = 2\pi T/T_{RT}$, so that $\frac{\partial^2}{\partial T^2} = \left(\frac{2\pi}{T_{RT}}\right)^2 \frac{\partial^2}{\partial \theta^2}$, and after dividing by T_{RT} we have:

$$\frac{\partial A}{\partial t} = -\frac{\Delta\omega}{2}A + \frac{1}{T_{RT}}(i\phi_{RT} + i\gamma|A|^2)A - i\frac{1}{T_{RT}}\left(\frac{2\pi}{T_{RT}}\right)^2 \frac{k''}{2}\frac{\partial^2 A}{\partial \theta^2} + A_{in}/\sqrt{T_{RT}\tau_{ext}} \quad (\text{A.7})$$

Dividing by $\Delta\omega/2$ brings us to the normalized temporal variable $\tau = t/2\tau_{ph} = \Delta\omega t/2$. The quantity ϕ_{RT}/T_{RT} is exactly the frequency detuning $\sigma = \omega_p - \omega_0$ between the pump laser and the cavity resonance frequency, so that the quantity $2\phi_{RT}/T_{RT}\Delta\omega$ that results from division by $\Delta\omega/2$ is simply equal to the normalized detuning $\alpha = -2\sigma/\Delta\omega$. Further, recalling from Sec. 1.2.1 that $D_1 = 2\pi/T_{RT} = 2\pi v_g/L$ and $D_2 = -D_1^2 v_g k''$, we have:

$$\frac{1}{2}\left(\frac{2\pi}{T_{RT}}\right)^2 \frac{k''}{T_{RT}} = -D_2/2. \quad (\text{A.8})$$

Using the definition of the normalized dispersion for the LLE $\beta_2 = -2D_2/\Delta\omega$ and combining these relations, we have:

$$\frac{\partial A}{\partial \tau} = -(1 + i\alpha)A + i\frac{2L\gamma}{T_{RT}\Delta\omega}|A|^2 A - i\frac{\beta_2}{2}\frac{\partial^2 A}{\partial \theta^2} + \sqrt{\frac{4\Delta\omega_{ext}}{T_{RT}\Delta\omega^2}} A_{in}, \quad (\text{A.9})$$

where we recall the definition $\Delta\omega_{ext} = 1/\tau_{ext}$. By defining $\psi = \sqrt{\frac{2L\gamma}{T_{RT}\Delta\omega}} A$, we can arrive at the LLE as presented in Eq. 1.11:

$$\frac{\partial \psi}{\partial \tau} = -(1 + i\alpha)\psi + i|\psi|^2\psi - i\frac{\beta_2}{2}\frac{\partial^2 \psi}{\partial \theta^2} + F. \quad (\text{A.10})$$

Here the pump term has been normalized as:

$$F = A_{in}\sqrt{\frac{8L\gamma\Delta\omega_{ext}}{T_{RT}^2\Delta\omega^3}} \quad (\text{A.11})$$

$$= A_{in}\sqrt{\frac{8g_0\Delta\omega_{ext}}{\Delta\omega^3}} \frac{1}{\hbar\omega_p}, \quad (\text{A.12})$$

with

$$g_0 = n_2 c \hbar \omega_p^2 / n_g^2 V_0, \quad (\text{A.13})$$

as defined in Sec. 1.2.1, where $V_0 = LA_{eff}$. Assuming that A_{in} is real simply fixes the phase of ψ , which is otherwise arbitrary. With this assumption we have $A_{in} = \sqrt{P_{in}}$, and we recover the relationship from Sec. 1.2.1:

$$F = \sqrt{\frac{8g_0\Delta\omega_{ext}}{\Delta\omega^3}} \frac{P_{in}}{\hbar\omega_p}. \quad (\text{A.14})$$

References

- [1] P Del’Haye, A Schliesser, O Arcizet, T Wilken, R Holzwarth, and T. J. Kippenberg. Optical frequency comb generation from a monolithic microresonator. *Nature*, 450 (7173), **2007**, 1214–1217. DOI: 10.1038/nature06401 (cited on pages 1, 6).
- [2] T. J. Kippenberg, R Holzwarth, and S. A. Diddams. Microresonator-Based Optical Frequency Combs. *Science (New York, N.Y.)*, 332 (6029), **2011**, 555–559. DOI: 10.1126/science.1193968 (cited on pages 1, 6).
- [3] A. A. Savchenkov, A. B. Matsko, and L Maleki. On Frequency Combs in Monolithic Resonators. *Nanophotonics*, 5, **2016**, 363–391. DOI: 10.1515/nanoph-2016-0031 (cited on page 1).
- [4] Y. K. Chembo. Kerr optical frequency combs: Theory, applications and perspectives. *Nanophotonics*, 5 (2), **2016**, 214–230. DOI: 10.1515/nanoph-2016-0013 (cited on page 1).
- [5] A. Pasquazi, M. Peccianti, L. Razzari, D. J. Moss, S. Coen, M. Erkintalo, Y. K. Chembo, T. Hansson, S. Wabnitz, P. Del’Haye, X. Xue, A. M. Weiner, and R. Morandotti. Micro-combs: A novel generation of optical sources. *Physics Reports*, 729, **2017**, 1–81. DOI: 10.1016/j.physrep.2017.08.004 (cited on page 1).
- [6] H. Lee, T. Chen, J. Li, K. Y. Yang, S. Jeon, O. Painter, and K. J. Vahala. Chemically etched ultrahigh-Q wedge-resonator on a silicon chip. *Nature Photonics*, 6 (6), **2012**, 369–373. DOI: 10.1038/nphoton.2012.109. arXiv: 1112.2196 (cited on pages 1, 2).
- [7] X. Yi, Q.-F. Yang, K. Y. Yang, M.-G. Suh, and K. Vahala. Soliton frequency comb at microwave rates in a high-Q silica microresonator. *Optica*, 2 (12), **2015**, 1078–1085 (cited on pages 1, 16).
- [8] P. Del’Haye, S. A. Diddams, and S. B. Papp. Laser-machined ultra-high-Q microrod resonators for nonlinear optics. *Applied Physics Letters*, 102, **2013**, 221119 (cited on pages 1, 3).
- [9] W Liang, A. A. Savchenkov, A. B. Matsko, V. S. Ilchenko, D Seidel, and L Maleki. Generation of near-infrared frequency combs from a MgF₂ whispering gallery mode resonator. *Optics Letters*, 36 (12), **2011**, 2290–2292. DOI: 10.1364/OL.36.002290 (cited on page 1).
- [10] A. a. Savchenkov, A. B. Matsko, V. S. Ilchenko, I. Solomatine, D. Seidel, and L. Maleki. Tunable optical frequency comb with a crystalline whispering gallery mode resonator. *Physical Review Letters*, 101 (9), **2008**, 1–4. DOI: 10.1103/PhysRevLett.101.093902. arXiv: 0804.0263 (cited on page 1).
- [11] Y. Okawachi, K. Saha, J. S. Levy, Y. H. Wen, M. Lipson, and A. L. Gaeta. Octave-spanning frequency comb generation in a silicon nitride chip. *Optics Letters*, 36 (17), **2011**, 3398–3400. DOI: 10.1364/OL.36.003398. arXiv: 1107.5555 (cited on page 1).
- [12] D. J. Moss, R Morandotti, A. L. Gaeta, and M Lipson. New CMOS-compatible platforms based on silicon nitride and Hydex for nonlinear optics. *Nature Photonics*, 7 (July), **2013**, 597–607. DOI: 10.1038/nphoton.2013.183 (cited on page 1).
- [13] D. Braje, L. Hollberg, and S. Diddams. Brillouin-Enhanced Hyperparametric Generation of an Optical Frequency Comb in a Monolithic Highly Nonlinear Fiber Cavity Pumped by a cw Laser. *Physical Review Letters*, 102 (19), **2009**, 193902. DOI: 10.1103/PhysRevLett.102.193902 (cited on page 1).

- [14] E. Obrzud, S. Lecomte, and T. Herr. Temporal solitons in microresonators driven by optical pulses. *Nature Photonics*, 11 (August), **2017**, 600–607. DOI: 10.1038/nphoton.2017.140. arXiv: 1612.08993 (cited on pages 1, 16).
- [15] V. S. Ilchenko and A. B. Matsko. Optical resonators with whispering-gallery modes - Part II: Applications. *IEEE Journal on Selected Topics in Quantum Electronics*, 12 (1), **2006**, 15–32. DOI: 10.1109/JSTQE.2005.862943 (cited on page 1).
- [16] K. Y. Yang, K. Beha, D. C. Cole, X. Yi, P. Del’Haye, H. Lee, J. Li, D. Y. Oh, S. A. Diddams, S. B. Papp, and K. J. Vahala. Broadband dispersion-engineered microresonator on a chip. *Nature Photonics*, 10 (March), **2016**, 316–320. DOI: 10.1038/nphoton.2016.36 (cited on page 2).
- [17] G. P. Agrawal. **Nonlinear Fiber Optics**. 4th. Burlington, MA: Elsevier, 2007 (cited on pages 2, 6–8, 13, 18).
- [18] M. L. Calvo and V. Lakshminarayanan, eds. **Optical Waveguides: From Theory to Applied Technologies**. Boca Raton, FL: Taylor & Francis, 2007 (cited on page 2).
- [19] A. N. Oraevsky. Whispering-gallery waves. *Quantum Electronics*, 32 (42), **2002**, 377–400. DOI: 10.1070/QE2001v031n05ABEH002205. arXiv: arXiv:1011.1669v3 (cited on page 3).
- [20] H. A. Haus. **Waves and Fields in Optoelectronics**. Englewood Cliffs: Prentice-Hall, 1984 (cited on page 3).
- [21] J. C. Knight, G. Cheung, F. Jacques, and T. A. Birks. Phase-matched excitation of whispering-gallery-mode resonances by a fiber taper. *Optics Letters*, 22 (15), **1997**, 1129. DOI: 10.1364/OL.22.001129 (cited on page 4).
- [22] S. M. Spillane, T. J. Kippenberg, O. J. Painter, and K. J. Vahala. Ideality in a Fiber-Taper-Coupled Microresonator System for Application to Cavity Quantum Electrodynamics. *Physical review letters*, 91 (4), **2003**, 043902. DOI: 10.1103/PhysRevLett.91.043902 (cited on page 4).
- [23] E. Shah Hosseini, S. Yegnanarayanan, A. H. Atabaki, M. Soltani, and A. Adibi. Systematic design and fabrication of high-Q single-mode pulley-coupled planar silicon nitride microdisk resonators at visible wavelengths. *Optics Express*, 18 (3), **2010**, 2127. DOI: 10.1364/OE.18.002127 (cited on page 4).
- [24] T. Carmon, L. Yang, and K. J. Vahala. Dynamical thermal behavior and thermal self-stability of microcavities. *Optics Express*, 12 (20), **2004**, 4742–4750. URL: <http://www.ncbi.nlm.nih.gov/pubmed/19484026><http://www.opticsinfobase.org/oe/abstract.cfm?uri=oe-12-20-4742> (cited on page 4).
- [25] R. W. Boyd. **Nonlinear Optics**. San Diego, CA: Elsevier, 2003 (cited on page 6).
- [26] R. del Coso and J. Solis. Relation between nonlinear refractive index and third-order susceptibility in absorbing media. *Journal of the Optical Society of America B*, 21 (3), **2004**, 640. DOI: 10.1364/JOSAB.21.000640 (cited on page 6).
- [27] T. Kippenberg, S. Spillane, and K. Vahala. Kerr-Nonlinearity Optical Parametric Oscillation in an Ultrahigh-Q Toroid Microcavity. *Physical Review Letters*, 93 (8), **2004**, 083904. DOI: 10.1103/PhysRevLett.93.083904 (cited on page 6).
- [28] A. A. Savchenkov, A. B. Matsko, D. Strekalov, M. Mohageg, V. S. Ilchenko, and L. Maleki. Low threshold optical oscillations in a whispering gallery mode CaF₂ resonator. *Physical Review Letters*, 93 (24), **2004**, 2–5. DOI: 10.1103/PhysRevLett.93.243905 (cited on page 6).
- [29] I. H. Agha, Y. Okawachi, M. A. Foster, J. E. Sharping, and A. L. Gaeta. Four-wave-mixing parametric oscillations in dispersion-compensated high-Q silica microspheres. *Physical Review A - Atomic, Molecular, and Optical Physics*, 76 (4), **2007**, 1–4. DOI: 10.1103/PhysRevA.76.043837 (cited on page 6).
- [30] T. Herr, V. Brasch, J. D. Jost, C. Y. Wang, N. M. Kondratiev, M. L. Gorodetsky, and T. J. Kippenberg. Temporal solitons in optical microresonators. *arXiv*, **2012**, 1211.0733. DOI: 10.1038/nphoton.2013.343. arXiv: 1211.0733 (cited on pages 6, 16).

- [31] T. Herr, V. Brasch, J. D. Jost, C. Y. Wang, N. M. Kondratiev, M. L. Gorodetsky, and T. J. Kippenberg. Temporal solitons in optical microresonators. *Nature Photonics*, 8 (2), **2014**, 145–152. DOI: 10.1109/CLEOE-IQEC.2013.6801769. arXiv: 1211.0733 (cited on pages 6, 8, 14–16).
- [32] F. Leo, S. Coen, P. Kockaert, S.-P. Gorza, P. Emplit, and M. Haelterman. Temporal cavity solitons in one-dimensional Kerr media as bits in an all-optical buffer. *Nature Photonics*, 4 (7), **2010**, 471–476. DOI: 10.1038/nphoton.2010.120 (cited on page 6).
- [33] T. Herr, K. Hartinger, J. Riemensberger, C. Y. Wang, E. Gavartin, R. Holzwarth, M. L. Gorodetsky, and T. J. Kippenberg. Universal formation dynamics and noise of Kerr-frequency combs in microresonators. *Nature Photonics*, 6 (7), **2012**, 480–487. DOI: 10.1038/nphoton.2012.127 (cited on page 7).
- [34] Y. K. Chembo and C. R. Menyuk. Spatiotemporal Lugiato-Lefever formalism for Kerr-comb generation in whispering-gallery-mode resonators. *Physical Review A*, 87, **2013**, 053852. DOI: 10.1103/PhysRevA.87.053852 (cited on page 7).
- [35] S. Coen, H. G. Randle, T. Sylvestre, and M. Erkintalo. Modeling of octave-spanning Kerr frequency combs using a generalized mean-field Lugiato-Lefever model. *Optics letters*, 38 (1), **2013**, 37–39. URL: <http://www.ncbi.nlm.nih.gov/pubmed/23282830> (cited on pages 7, 8).
- [36] M. Haelterman, S. Trillo, and S. Wabnitz. Dissipative modulation instability in a nonlinear dispersive ring cavity. *Optics Communications*, 91 (5-6), **1992**, 401–407. DOI: 10.1016/0030-4018(92)90367-Z (cited on pages 7, 18).
- [37] T. Hansson, M. Bernard, and S. Wabnitz. Modulational Instability of Nonlinear Polarization Mode Coupling in Microresonators. 35 (4), **2018**. URL: <https://arxiv.org/pdf/1802.04535.pdf>. arXiv: arXiv:1802.04535v1 (cited on page 8).
- [38] Y. K. Chembo, I. S. Grudinin, and N. Yu. Spatiotemporal dynamics of Kerr-Raman optical frequency combs. *Physical Review A*, 92 (4), **2015**, 4. DOI: 10.1103/PhysRevA.92.043818 (cited on page 8).
- [39] C. Godey, I. V. Balakireva, A. Coillet, and Y. K. Chembo. Stability analysis of the spatiotemporal Lugiato-Lefever model for Kerr optical frequency combs in the anomalous and normal dispersion regimes. *Physical Review A*, 89 (6), **2014**, 063814. DOI: 10.1103/PhysRevA.89.063814 (cited on pages 8, 9, 11).
- [40] I. V. Barashenkov and Y. S. Smirnov. Existence and stability chart for the ac-driven, damped nonlinear Schrödinger solitons. *Physical Review E - Statistical Physics, Plasmas, Fluids, and Related Interdisciplinary Topics*, 54 (5), **1996**, 5707–5725. DOI: 10.1103/PhysRevE.54.5707 (cited on pages 8, 15).
- [41] A. Coillet and Y. K. Chembo. Routes to spatiotemporal chaos in Kerr optical frequency combs. *Chaos*, 24 (1), **2014**, 5. DOI: 10.1063/1.4863298. arXiv: arXiv:1401.0927v1 (cited on page 11).
- [42] L. A. Lugiato and R. Lefever. Spatial Dissipative Structures in Passive Optical Systems. *Physical Review Letters*, 58 (21), **1987**, 2209–2211 (cited on pages 11, 13).
- [43] L. Lugiato and R. Lefever. Diffraction stationary patterns in passive optical systems. *Interaction of Radiation with Matter*, **1987** (cited on page 11).
- [44] W. H. Renninger and P. T. Rakich. Closed-form solutions and scaling laws for Kerr frequency combs. *Scientific Reports*, 6 (1), **2016**, 24742. DOI: 10.1038/srep24742. arXiv: 1412.4164 (cited on page 11).
- [45] J. S. Russell. Report on Waves. *Fourteenth meeting of the British Association for the Advancement of Science*, **1844**, 311–390 (cited on page 13).
- [46] M. Brambilla, L. A. Lugiato, F. Prati, L. Spinelli, and W. J. Firth. Spatial soliton pixels in semiconductor devices. *Physical Review Letters*, 79 (11), **1997**, 2042–2045. DOI: 10.1103/PhysRevLett.79.2042 (cited on page 13).

- [47] S. Minardi, F. Eilenberger, Y. V. Kartashov, A. Szameit, U. Röpke, J. Kobelke, K. Schuster, H. Bartelt, S. Nolte, L. Torner, F. Lederer, A. Tünnermann, and T. Pertsch. Three-dimensional light bullets in arrays of waveguides. *Physical Review Letters*, 105 (26), **2010**, 1–4. DOI: 10.1103/PhysRevLett.105.263901. arXiv: 1101.0734 (cited on page 13).
- [48] F. X. Kärtner, I. D. Jung, and U. Keller. Soliton mode-locking with saturable absorbers. *IEEE Journal on Selected Topics in Quantum Electronics*, 2 (3), **1996**, 540–556. DOI: 10.1109/2944.571754 (cited on page 13).
- [49] P. Grelu and N. Akhmediev. Dissipative solitons for mode-locked lasers. *Nature Photonics*, 6 (February), **2012**, 84–92. DOI: 10.1109/PGC.2010.5706017 (cited on page 13).
- [50] L. F. Mollenauer and J. P. Gordon. **Solitons in Optical Fibers**. Academic Press, 2006, p. 296 (cited on page 13).
- [51] A. Hasegawa and Y. Kodama. **Solitons in Optical Communications**. Academic Press, 1995 (cited on page 13).
- [52] H. A. Haus and W. S. Wong. Solitons in optical communications. *Reviews of Modern Physics*, 68 (2), **1996**, 423–444. DOI: 10.1103/RevModPhys.68.423 (cited on page 13).
- [53] S. Coen and M. Erkintalo. Universal scaling laws of Kerr frequency combs. *Optics letters*, 38 (11), **2013**, 1790–1792. DOI: 10.1364/OL.38.001790. arXiv: arXiv:1303.7078v1 (cited on page 15).
- [54] H. Guo, M. Karpov, E. Lucas, A. Kordts, M. H. Pfeiffer, V. Brasch, G. Lihachev, V. E. Lobanov, M. L. Gorodetsky, and T. J. Kippenberg. Universal dynamics and deterministic switching of dissipative Kerr solitons in optical microresonators. *Nature Physics*, 13 (1), **2017**, 94–102. DOI: 10.1038/nphys3893. arXiv: 1601.05036 (cited on pages 15, 16).
- [55] N. J. Zabusky and M. D. Kruskal. Interaction of "solitons" in a collisionless plasma and the recurrence of initial states. *Physical Review Letters*, 15 (6), **1965**, 240 (cited on page 15).
- [56] J. P. Gordon. Interaction forces among solitons in optical fibers. *Optics Letters*, 8 (11), **1983**, 596. DOI: 10.1364/OL.8.000596 (cited on page 15).
- [57] B. A. Malomed. Bound solitons in the nonlinear Schrodinger-Ginzburg-Landau equation. *Physical Review A*, 44 (10), **1991**, 6954–6957. DOI: 10.1103/PhysRevA.44.6954 (cited on page 15).
- [58] J. K. Jang, M. Erkintalo, S. G. Murdoch, and S. Coen. Ultraweak long-range interactions of solitons observed over astronomical distances. *Nature Photonics*, 7 (8), **2013**, 657–663. DOI: 10.1038/nphoton.2013.157. arXiv: arXiv:1305.6670v1 (cited on page 15).
- [59] P. Parra-Rivas, D. Gomila, P. Colet, and L. Gelens. Interaction of solitons and the formation of bound states in the generalized Lugiato-Lefever equation. *European Physical Journal D*, 71 (7), **2017**, 198. DOI: 10.1140/epjd/e2017-80127-5. arXiv: arXiv:1705.02619v1 (cited on page 15).
- [60] Y. Wang, F. Leo, J. Fatome, M. Erkintalo, S. G. Murdoch, and S. Coen. Universal mechanism for the binding of temporal cavity solitons, **2017**, 1–10. URL: <http://arxiv.org/abs/1703.10604>. arXiv: 1703.10604 (cited on page 15).
- [61] V. Brasch, T. Herr, M. Geiselmann, G. Lihachev, M. H. P. Pfeiffer, M. L. Gorodetsky, and T. J. Kippenberg. Photonic chip-based optical frequency comb using soliton Cherenkov radiation. *Science*, 351 (6271), **2016**, 357. DOI: 10.1364/CLEO_SI.2015.STh4N.1. arXiv: 1410.8598 (cited on page 16).
- [62] J. R. Stone, T. C. Briles, T. E. Drake, D. T. Spencer, D. R. Carlson, S. A. Diddams, and S. B. Papp. Thermal and Nonlinear Dissipative-Soliton Dynamics in Kerr Microresonator Frequency Combs. *arXiv*, **2017**, 1708.08405. URL: <http://arxiv.org/abs/1708.08405>. arXiv: 1708.08405 (cited on page 16).
- [63] V. E. Lobanov, G. V. Lihachev, N. G. Pavlov, A. V. Cherenkov, T. J. Kippenberg, and M. L. Gorodetsky. Harmonization of chaos into a soliton in Kerr frequency combs. *Optics Express*, 24 (24), **2016**, 27382. DOI: 10.1126/science.aah4243. arXiv: 1607.08222 (cited on page 16).

- [64] C. Joshi, J. K. Jang, K. Luke, X. Ji, S. A. Miller, A. Klenner, Y. Okawachi, M. Lipson, and A. L. Gaeta. Thermally controlled comb generation and soliton modelocking in microresonators. *Optics Letters*, 41 (11), **2016**, 2565–2568. DOI: 10.1364/OL.41.002565. arXiv: 1603.08017 (cited on page 16).
- [65] W. Wang, Z. Lu, W. Zhang, S. T. Chu, B. E. Little, L. Wang, X. Xie, M. Liu, Q. Yang, L. Wang, J. Zhao, G. Wang, Q. Sun, Y. Liu, Y. Wang, and W. Zhao. Robust soliton crystals in a thermally controlled microresonator. *Optics Letters*, 43 (9), **2018**, 2002–2005. DOI: 10.1364/OL.43.002002 (cited on page 16).
- [66] J. K. Jang, M. Erkintalo, S. G. Murdoch, and S. Coen. Writing and erasing of temporal cavity solitons by direct phase modulation of the cavity driving field. *Optics Letters*, 40 (20), **2015**, 4755–4758. DOI: 10.1364/OL.40.004755. arXiv: 1501.05289 (cited on page 16).
- [67] J. K. Jang, M. Erkintalo, S. Coen, and S. G. Murdoch. Temporal tweezing of light through the trapping and manipulation of temporal cavity solitons. *Nature Communications*, 6, **2015**, 7370. DOI: 10.1038/ncomms8370. arXiv: 1410.4836 (cited on page 16).
- [68] Y. Wang, B. Garbin, F. Leo, S. Coen, M. Erkintalo, and S. G. Murdoch. Writing and Erasure of Temporal Cavity Solitons via Intensity Modulation of the Cavity Driving Field. *arXiv*, **2018**, 1802.07428. arXiv: 1802.07428 (cited on page 16).
- [69] S. B. Papp, K. Beha, P. Del’Haye, F. Quinlan, H. Lee, K. J. Vahala, and S. A. Diddams. Microresonator frequency comb optical clock. *Optica*, 1 (1), **2014**, 10–14. DOI: 10.1364/OPTICA.1.000010. arXiv: 1309.3525 (cited on page 17).
- [70] M. G. Suh, Q. F. Yang, K. Y. Yang, X. Yi, and K. J. Vahala. Microresonator soliton dual-comb spectroscopy. *Science*, 354 (6312), **2016**, 1–5. DOI: 10.1126/science.aah6516. arXiv: 1607.08222 (cited on page 17).
- [71] P. Marin-Palomo, J. N. Kemal, M. Karpov, A. Kordts, J. Pfeifle, M. H. Pfeiffer, P. Trocha, S. Wolf, V. Brasch, M. H. Anderson, R. Rosenberger, K. Vijayan, W. Freude, T. J. Kippenberg, and C. Koos. Microresonator-based solitons for massively parallel coherent optical communications. *Nature*, 546 (7657), **2017**, 274–279. DOI: 10.1038/nature22387. arXiv: 1610.01484 (cited on page 17).
- [72] D. T. Spencer, T. Drake, T. C. Briles, J. Stone, L. C. Sinclair, C. Fredrick, Q. Li, D. Westly, B. R. Illic, A. Bluestone, N. Volet, T. Komljenovic, L. Chang, S. H. Lee, D. Y. Oh, T. J. Kippenberg, E. Norberg, L. Theogarajan, M.-g. Suh, K. Y. Yang, H. P. Martin, K. Vahala, N. R. Newbury, K. Srinivasan, J. E. Bowers, S. A. Diddams, and S. B. Papp. An optical-frequency synthesizer using integrated photonics. *Nature*, 557, **2018**, 81–85. DOI: 10.1038/s41586-018-0065-7 (cited on page 17).
- [73] J. D. Jost, T. Herr, C. Lecaplain, V. Brasch, M. H. P. Pfeiffer, and T. J. Kippenberg. Counting the cycles of light using a self-referenced optical microresonator. *Optica*, 2 (8), **2015**, 706–711. DOI: 10.1364/OPTICA.2.000706. arXiv: 1411.1354 (cited on page 17).
- [74] P. Del’Haye, A. Coillet, T. Fortier, K. Beha, D. C. Cole, K. Y. Yang, H. Lee, K. J. Vahala, S. B. Papp, and S. A. Diddams. Phase-coherent microwave-to-optical link with a self-referenced microcomb. *Nature Photonics*, 10 (June), **2016**, 1–5. DOI: 10.1038/nphoton.2016.105 (cited on page 17).
- [75] V. Brasch, E. Lucas, J. D. Jost, M. Geiselmann, and T. J. Kippenberg. Self-referenced photonic chip soliton Kerr frequency comb. *Light: Science & Applications*, 6 (1), **2017**, e16202. DOI: 10.1038/lsa.2016.202. arXiv: 1605.02801 (cited on page 17).
- [76] T. C. Briles, J. R. Stone, T. E. Drake, D. T. Spencer, C. Frederick, Q. Li, D. A. Westly, B. R. Illic, K. Srinivasan, S. A. Diddams, and S. B. Papp. Kerr-microresonator solitons for accurate carrier-envelope-frequency stabilization. *arXiv*, **2017**, 1711.06251. URL: <http://arxiv.org/abs/1711.06251>. arXiv: 1711.06251 (cited on page 17).